Nanoscale

PAPER

View Article Online
View Journal | View Issue

Cite this: *Nanoscale*, 2024, **16**, 19763

Chemical activation of atom-precise Pd_3 nanoclusters on γ-Al_2O_3 supports for transfer hydrogenation reactions†

Siddhant Singh,[a] Dami Wi,[a] Kholoud E. Salem,[b] Drew Higgins[b] and Robert W. J. Scott *[a]

Received 15th August 2024,
Accepted 30th September 2024

DOI: 10.1039/d4nr03364g

rsc.li/nanoscale

Deposition of atom-precise nanoclusters onto solid supports is a promising route to synthesize model heterogeneous catalysts. However, to enhance nanocluster-support interactions, activation of the nanoclusters by removal of surface ligands is necessary. Thermal treatment to remove surface ligands from supported metal nanoclusters can yield highly active heterogeneous catalysts, however, the high temperatures employed can lead to poor control over the final size and speciation of the nanoclusters. As an alternative to high-temperature thermal treatments, chemical activation of $[Pd_3(\mu\text{-}Cl)(\mu\text{-}PPh_2)_2(PPh_3)_3]^+$ (Pd_3) nanoclusters on γ-Al_2O_3 supports under mild reaction conditions has been demonstrated in this work. Hydride-based reducing agents such as $NaBH_4$, $LiBH_4$, and $LiAlH_4$ have been examined for the activation of the Pd_3 nanoclusters. The structural evolution and speciation of the nanoclusters after activation have been monitored using a combination of XAS, XPS, STEM-EDX mapping, and solid-state NMR techniques. The results indicate that treatment with borohydride reducing agents successfully removed surface phosphine and chloride ligands, and the extent of size growth of the nanoclusters during activation is directly correlated with the amount of borohydride used. Borate side products remain on the γ-Al_2O_3 surface after activation; moreover, exposure to high amounts of $NaBH_4$ resulted in the incorporation of B atoms inside the lattice of the activated Pd nanoclusters. $LiAlH_4$ treatment, on the other hand, led to no significant size growth of the nanoclusters and resulted in a mixture of Pd single-atom sites and activated nanoclusters on the γ-Al_2O_3 surface. Finally, the catalytic potential of the activated nanoclusters has been tested in the transfer hydrogenation of *trans*-cinnamaldehyde, using sodium formate/formic acid as the hydrogen donor. The catalytic results showed that smaller Pd nanoclusters are much more selective for hydrogenating *trans*-cinnamaldehyde to hydrocinnamaldehyde, but overall have lower activity compared to larger Pd nanoparticles. Overall, this study showcases chemical activation routes as an alternative to traditional thermal activation routes for activating supported nanoclusters by offering improved speciation and size control.

Introduction

Solid-supported nanoclusters (NCs) of Pd are highly selective and active catalysts for essential catalytic processes such as the selective hydrogenation of alkynes (*e.g.*, acetylene), CO oxidation, C–C coupling, and dehydrogenation reactions.[1–6] The high catalytic selectivity and activity of NCs can be attributed to their large surface area and the size-dependent arrangement of surface atoms.[3–5] One common strategy to obtain solid-supported NCs is the deposition of pre-synthesized ligand-protected atom-precise NCs onto a support material followed by activation (*i.e.*, removal of surface ligands).[5,7,8] Bottom-up, surface ligand-assisted synthetic approaches have enabled structural control over atom-precise NCs which contain well-defined metal cores with surface ligands coating the metal core.[9] However, upon immobilization of NCs on solid supports (*i.e.*, solid-supported NCs) for heterogeneous catalytic processes, their surface ligands can prevent strong support–NC interactions and also act as a barrier for substrates to access catalytically active metal surfaces during catalytic processes.[8,10] Therefore, atom-precise NCs are first deposited on a suitable solid support followed by removing the surface ligands from the NCs in a subsequent activation step.[7,8,10] A central ques-

[a]*Department of Chemistry, University of Saskatchewan, 110 Science Place, Saskatoon, Saskatchewan S7N 5C9, Canada. E-mail: robert.scott@usask.ca*
[b]*Department of Chemical Engineering, McMaster University, 1280 Main St W, Hamilton, Ontario L8S 4L7, Canada*

† Electronic supplementary information (ESI) available. See DOI: https://doi.org/10.1039/d4nr03364g

tion in the field is how to effectively remove the ligands from the surface of pre-fabricated NCs with minimum distortion in the structure and size of the NCs.[10–12]

$[Pd_3(\mu\text{-}Cl)(\mu\text{-}PPh_2)_2(PPh_3)_3]^+$ (abbreviated hereafter as Pd_3) NCs have shown promising catalytic activity and selectivity in cross-coupling reactions when used without immobilization on solid supports.[13,14] However, a recent study by Fairlamb and coworkers suggested that non-immobilized Pd_3 NCs are less stable during cross-coupling reactions compared to resin-immobilized Pd_3 NCs.[6] Yun *et al.* demonstrated that non-immobilized Pd_3 NCs are almost inactive catalysts for the oxidation of benzyl alcohol, however, upon immobilizing the Pd_3 NCs on titanate nanotubes, a remarkable increase in their activity was observed due to metal–support interactions.[15] These studies suggest that immobilizing Pd_3 NCs onto solid supports not only stabilizes the NCs but can also significantly enhance their catalytic potential.[6,15] Our group previously reported the immobilization of Pd_3 NCs onto activated carbon supports for hydrogenation and cross-coupling reactions, and found that Pd_3 NCs adsorbed on activated carbon supports do not behave as true heterogeneous catalysts, as intact Pd_3 NCs leached into the reaction mixture during cross-coupling reactions.[16] Thus the presence of phosphine ligands on the Pd_3 NCs hindered strong interactions between NCs and the support. However, thermal activation of Pd_3 NCs in the air led to the complete removal of surface ligands, resulting in catalysts that exhibited true heterogeneous behavior.[16] While the thermal activation of NCs is a straightforward strategy, drawbacks associated with this strategy include uncontrolled sintering of NCs to larger nanoparticles (NPs), particularly at higher activation temperatures.[16–20] Additionally, many metals, including Pd, tend to oxidize and form metal oxides at moderate temperatures of thermal activation.[16,20] Therefore due to the poor speciation and morphology control over NCs during thermal activation, the catalytic potential of the NCs can be adversely affected.[10,16]

An alternative method to activate NCs is through chemical activation, where ligands are removed from the surface of the NCs following chemical treatment.[10,21] One of the most promising strategies for chemically activating NCs involves treating them with reducing agents.[10] This process includes the reduction of surface ligands, which are subsequently removed as free ligands.[10] Collins *et al.* have shown a comparison between the thermal and reductive chemical activation of oleylamine, dodecanethiol, and polyvinylpyrrolidone-stabilized Pd NPs.[22] They found that the chemical activation of Pd NPs using $NaBH_4$ was less effective in completely removing strongly binding ligands such as dodecanethiol from the surfaces of NPs than thermal activation routes.[22] However, the chemically activated NPs were found to be more catalytically active in cross-coupling reactions compared to both non-activated and thermally activated NPs.[22] Several groups, including our own, have previously shown that thiolate monolayer-protected Au NCs can be reductively activated in the presence of excessive borohydride reducing agents, and the post-activation size growth of NCs directly depends upon both the concentrations and strength of reducing agents used for the activation.[23–25] For example, the activation of γ-Al_2O_3-supported $Au_{25}(SC_8H_9)_{18}$ NCs with an excess of $NaBH_4$ led to the partial removal of thiolates from the Au NCs and resulted in minimal size growth of Au NCs.[25] Zhang and co-workers noted that hydrides exhibit a higher binding affinity to the surface of Au compared to organothiolate ligands, and consequently, an excess of hydride species can displace surface ligands from precious metals.[26] To the best of our knowledge, reductive chemical routes toward the activation of Pd NCs have not yet been explored and require further investigation. Chemical activation pathways have the potential to act as an efficient way to activate Pd NCs while avoiding the sintering and oxidation of Pd NCs seen during thermal activation in air.[16]

In this study, the chemical activation of γ-Al_2O_3-supported atomically precise Pd_3 NCs using hydride-based reducing agents *i.e.*, $NaBH_4$, $LiBH_4$, and $LiAlH_4$, has been investigated. Various loadings of these reducing agents were examined to explore their impact on the activation process and subsequent structural changes of the NCs. The findings from this work indicate that all the selected reducing agents effectively removed phosphine and chloride ligands from the Pd_3 NC surfaces. In the case of $NaBH_4$ and $LiBH_4$, ligand removal was accompanied by very mild post-activation growth of the Pd_3 NCs at lower reducing agent amounts, while higher amounts of $NaBH_4$ during activation promoted the transformation of Pd_3 NCs into larger Pd NPs and led to the incorporation of B into the NPs. In contrast, $LiAlH_4$ treatment removed ligands from the Pd_3 NCs without any noticeable size growth, facilitating the formation of a mix of activated NCs and single-atom Pd sites on the γ-Al_2O_3 surface. The structural evolution of Pd_3 NCs during activation directly impacted the catalytic activity of the NCs, as demonstrated in their use as catalysts for the transfer hydrogenation of *trans*-cinnamaldehyde using sodium formate as the hydrogen donor. Smaller NCs exhibited high selectivity for hydrocinnamaldehyde formation, albeit with lower activity compared to larger Pd NPs. This work demonstrates the facile removal of phosphine and chloride ligands from Pd_3 NC surfaces *via* chemical means, highlighting how the choice and amount of the reducing agent used can lead to distinct structural transformations during activation.

Results and discussion

The synthesis, purification, and characterization of Pd_3 NCs were carried out following protocols established in the literature and our previous work.[16,27] Upon immobilization of the Pd_3 NCs on the surface of γ-Al_2O_3, the resulting composite has been denoted as Pd_3/Al_2O_3. Elemental analysis of the Pd_3/Al_2O_3 by atomic absorption spectroscopy showed a 0.5 wt% loading of the Pd on the γ-Al_2O_3 support. For chemical activations, three amounts of $NaBH_4$, $LiBH_4$, and $LiAlH_4$ have been used (as shown in Table S1†). Based on the reducing agents and their concentrations, the activated samples have been labelled as Pd/Al_2O_3-RA(x) (where RA is the used

reducing agent) (*i.e.*, $NaBH_4$, $LiBH_4$ or $LiAlH_4$) and *x* is the molar equivalents of the reducing agent used with respect to the Pd (labelled A, B, or C (Table S1†)). For the $NaBH_4$ reducing agent, 300 (A), 600 (B), or 1200 (C) mole equivalents were used for activation. Meanwhile, for $LiBH_4$ and $LiAlH_4$ reducing agents, 10 (A), 50 (B), and 100 (C) mole equivalents of the reducing agent were used for activation. The amounts of $NaBH_4$ used were larger because our previous work demonstrated that higher concentrations of aqueous $NaBH_4$ were necessary to activate thiolate-protected Au NCs compared to $LiBH_4$.[25]

To investigate the speciation and bonding environment of the NCs after chemical activation, XAS analysis has been performed. Pd K edge XANES spectra of all the activated samples have been provided in Fig. 1(a–c), along with Pd, PdO, and Pd $(OH)_2$ standards. Upon treatment with reducing agents, small changes in the shape of the white lines compared to the initial Pd_3/Al_2O_3 were observed. These changes indicate a modification in the speciation and coordination environment of the supported Pd NCs due to activation. In the case of Pd_3/Al_2O_3–$NaBH_4$(A) and Pd_3/Al_2O_3–$LiAlH_4$(A/B/C), the feature above the white line appeared slightly more intense compared to Pd_3/Al_2O_3, suggesting an increase in Pd(II) species. In contrast, the intensity of the sharp feature above the white line in the remaining $NaBH_4$ (Pd_3/Al_2O_3–$NaBH_4$(B/C)) and $LiBH_4$ (Pd_3/Al_2O_3–$LiBH_4$(A/B/C)) treated samples were found to be relatively lower, suggesting more Pd in the zerovalent state. However, the small XANES changes observed at the edge after activation suggest that XANES data does not offer detailed insights into the speciation changes within these systems. In contrast, changes detected by EXAFS (discussed below) are more informative.

To investigate the coordination environment of the activated Pd_3 NCs, EXAFS analysis at the Pd K edge was performed. The Fourier-transformed (FT) EXAFS spectra of activated samples along with the spectra of Pd_3/Al_2O_3 are provided in Fig. 1(d–f). In the spectra of Pd_3/Al_2O_3, a broad peak at around 1.6–1.8 Å can be seen due to the Pd–P and Pd–Cl interactions of the Pd core with the phosphine and chloride ligands. The small feature at around 2.7 Å can be assigned to Pd–Pd bonding in the triangular metal core of Pd_3 NCs. Notably, the Pd–Pd bond distance in Pd_3/Al_2O_3 was found to be slightly longer than that in fcc Pd, which is also the case in the reported single-crystal structure of Pd_3 NCs.[27] In the EXAFS spectra of all the activated NCs, an intense peak can be observed at 1.5 Å, which is shifted to the left in comparison to the Pd–P and Pd–Cl peak of the non-activated Pd_3/Al_2O_3 (at 1.6–1.8 Å). This suggests a complete removal of phosphines and chloride surface ligands from the metal core of the Pd_3 NCs upon activation; the peak at 1.5 Å in the Pd K edge EXAFS spectra is likely indicative of new Pd–O interaction. The appearance of this peak in activated samples indicates the interaction of Pd NCs with the basic surface oxygen sites of γ-Al_2O_3 after the removal of surface ligands from the Pd_3 NCs.

In the case of Pd_3/Al_2O_3–$NaBH_4$(A), the peak pertaining to the Pd–Pd interaction (originally at 2.7 Å) became less prominent in comparison to the Pd–Pd peak of Pd_3/Al_2O_3. This is

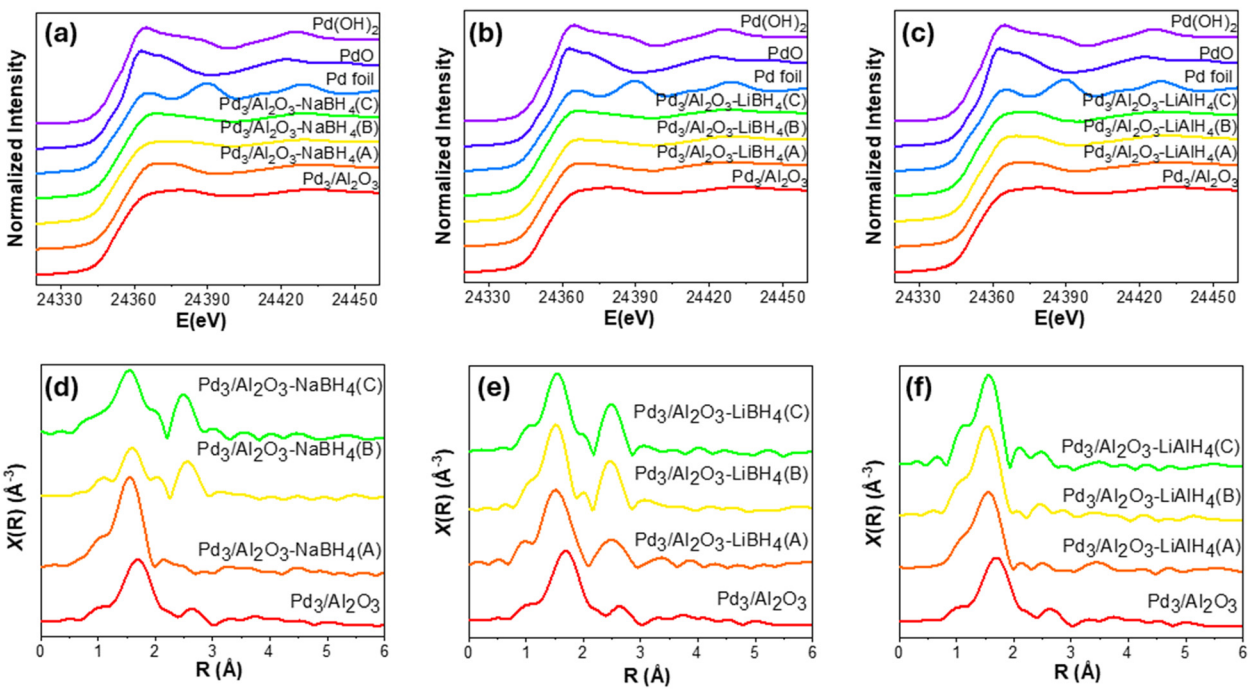

Fig. 1 Pd K-edge XANES spectra of the Pd_3/Al_2O_3 activated *via* treatment with different amounts of (a) $NaBH_4$, (b) $LiBH_4$ and (c) $LiAlH_4$ along with some standards. Pd K-edge Fourier transformed EXAFS spectra in *R*-space for Pd_3/Al_2O_3 activated *via* treatment with different amounts of (d) $NaBH_4$, (e) $LiBH_4$ and (f) $LiAlH_4$. All EXAFS spectra are shown without phase shift corrections.

likely due to the partial collapse of the triangular core of the Pd_3 NCs after the removal of surface ligands. Similar behaviour was previously observed with the carbon-supported Pd_3 NCs during their mild thermal activation at 150 °C.[16] With the use of higher amounts of $NaBH_4$ (*i.e.*, Pd_3/Al_2O_3–$NaBH_4$(B/C)) for activation, the peak for the Pd–Pd interactions around 2.6 Å became higher in intensity than seen for un-activated Pd_3/Al_2O_3, indicating an increase in the size of the Pd NCs during the activation. Meanwhile, the intensity of the Pd–O peak at around 1.5 Å in the spectra of Pd_3/Al_2O_3–$NaBH_4$(B/C) became lower in intensity compared to the corresponding Pd_3/Al_2O_3–$NaBH_4$(A). This implies the reduction in the Pd–O interaction between Pd and the support due to the growth in the size of the Pd NPs. Furthermore, the peak shapes in the 1.5–2.0 Å region in the FT EXAFS spectra of the Pd_3/Al_2O_3–$NaBH_4$(B/C) samples differ significantly from those observed in the Pd_3/Al_2O_3–$NaBH_4$(A) sample. However, confirming whether this change in peak shape is attributable to the presence of a second scatterer cannot be achieved by solely examining the FT EXAFS spectra. To further investigate the possibility of the presence of a second weak scatterer, wavelet transformed (WT) EXAFS spectra were generated.[28] In the WT EXAFS spectra of Pd_3/Al_2O_3–$NaBH_4$(A), a single peak can be seen at $R \sim 1.5$ Å (Fig. S1(c and d)†) across all the k range, which reflects the presence of a single scatter *i.e.*, O of the γ-Al_2O_3 support. However, in the cases of Pd_3/Al_2O_3–$NaBH_4$(B/C), significantly intense peaks around $R \sim 2.6$ Å from Pd–Pd interactions can be seen in the WT EXAFS data (Fig. S1 (e and g)†). Furthermore, in the region between R-values of 1.5 to 2.0 Å in the FT EXAFS spectra, two distinct peaks can be observed in different k-regions (0.5 to 8.5 and 8.5 to 12 $Å^{-1}$) of the WT EXAFS spectra, suggesting the probable existence of two scattering atoms (Fig. S1(f and h)†). Based on STEM-EDX mapping, solid-state NMR, and XPS analyses indicating the presence of B (with the B source being the borohydride-reducing agent) in these samples (*vide infra*), it is likely that the two scatterers are O and B.

In the FT EXAFS spectra of $LiBH_4$-treated samples (Pd_3/Al_2O_3–$LiBH_4$(A/B/C)) (Fig. 1e), the peaks of Pd–Pd interaction around 2.6 Å appeared to be higher in the intensity in comparison to Pd_3/Al_2O_3, reflecting a growth in the size of the Pd_3 NCs upon activation. The growth in the Pd–Pd peak became larger with an increase in the amount of $LiBH_4$ for activation (shown in Fig. 1e) suggesting the formation of larger Pd NCs with higher amounts of $LiBH_4$. All the WT EXAFS spectra of the $LiBH_4$-activated NCs (*i.e.*, Pd_3/Al_2O_3–$LiBH_4$(A/B/C)) (Fig. S2†) showed the presence of a single scatter for the first peak of the FT EXAFS around $R \sim 1.5$ Å. This affirms that Pd atoms in these systems are attached only to the O atoms of the surface of γ-Al_2O_3 after the activation, and no secondary scatterers are present. Moreover, another peak for the Pd–Pd interactions at around $R \sim 2.6$ Å in the WT EXAFS spectra can also be seen, which became more prominent with a further increase in the amount of the reducing agent. Finally, for Pd_3/Al_2O_3–$LiAlH_4$(A/B/C) (Fig. 1f), the FT EXAFS spectra showed that the peak corresponding to Pd–Pd interactions at 2.6–2.7 Å is nearly completely absent. This indicates that the triangular metal core of Pd_3 NCs has been broken after activation using $LiAlH_4$ without any significant size growth. Similar to the $LiBH_4$ treated samples, the $LiAlH_4$ treated samples have shown the presence of only one scatterer for the first peak at $R \sim 1.5$ Å in the WT EXAFS spectra (Fig. S3†), indicating the presence of Pd–O interactions. In addition, a very weak peak can be seen at around $R \sim 2.6$ Å for the Pd–Pd bonds.

EXAFS data modelling for these samples have been performed to get further insight into the structural evolution of the Pd_3 NCs upon activation. The k-space EXAFS fits for Pd_3/Al_2O_3 activated *via* different $NaBH_4$, $LiBH_4$, and $LiAlH_4$ amounts are shown in Fig. S4–S6,† respectively. The corresponding fitting parameters from the EXAFS fits can be found in Table 1. The fitting of the non-activated Pd_3/Al_2O_3 sample was carried out using Pd–P, Pd–Cl, and Pd–Pd interactions based on the structure of $[Pd_3(\mu\text{-}Cl)(\mu\text{-}PPh_2)_2(PPh_3)_3]^+$.[27] EXAFS fitting of the Pd_3/Al_2O_3 data provided coordination number (CN) values of 2.9 ± 0.3, 0.7 ± 0.3, and 1.8 ± 0.1 for Pd–P, Pd–Cl, and Pd–Pd bonds, respectively, which is quite consistent with the crystal structure of Pd_3 NCs.[27] The fitting of Pd_3/Al_2O_3–$NaBH_4$(A) suggested the presence of Pd–O contributions at a bond distance of 2.009 ± 0.001 Å with a CN value of 3.3 ± 0.1, likely due to metal–support interactions. Compared to Pd_3/Al_2O_3, a drop in the CN of Pd–Pd for this sample can be due to the distortion in the triangular core of the Pd_3 NCs upon activation. Since the WT EXAFS spectra of Pd_3/Al_2O_3–$NaBH_4$(B) and Pd_3/Al_2O_3–$NaBH_4$(C) (Fig. S1†) indicated the presence of two scatterers in the first coordination shell of Pd, and solid-state NMR and XPS also confirmed the presence of B in these two samples (*vide infra*), a Pd–B model has been chosen for fitting along with the Pd–O model for the peak present at $R \sim 1.5$ Å in the FT EXAFS of these two samples. B atoms are small enough to be intercalated inside the interstitial sites of the Pd fcc lattice.[29–31] In the literature, the use of borohydride reducing agents such as $(CH_3)_2NH{\cdot}BH_3$,[29] $NaBH_4$,[30] and $C_4H_8O{\cdot}BH_3$ [31] during the synthesis of Pd NPs has been reported to show the incorporation of B in the lattice of Pd NPs. Chen and co-workers have found that the B content in the Pd lattice can be directly correlated with the concentration of $NaBH_4$ used during the synthesis of Pd NPs.[30] From the EXAFS modelling, the CNs for Pd–O, Pd–B, and Pd–Pd interactions in Pd_3/Al_2O_3–$NaBH_4$(B) were 2.8 ± 0.1, 2.3 ± 0.6, and 2.4 ± 0.3, respectively. Bond lengths for the new Pd–B interactions were fitted at 1.87(3) Å and 1.98(2) Å, respectively, for the Pd_3/Al_2O_3–$NaBH_4$(B) and Pd_3/Al_2O_3–$NaBH_4$(C) samples. These Pd–B bond lengths are consistent with Pd–B bond lengths seen for PdB_x solid-state solutions, molecular complexes, and B-doped Pd NPs in the literature (*ca.* 1.9–2.2 Å).[32–34] In Pd_3/Al_2O_3–$NaBH_4$(C), the fitted CN values for Pd–B (3.3 ± 0.1) and Pd–Pd (4.0 ± 0.5) interactions are slightly higher than in the previous sample, while the CN for Pd–O has decreased significantly to 1.4 ± 0.3. This implies that as the amount of $NaBH_4$ used for activation increased, the size of the final Pd NPs also increased, along with the incorporation of B in the lattice of Pd NPs. The decrease in Pd–O inter-

Table 1 EXAFS fitting parameters of Pd_3/Al_2O_3 samples at the Pd K edge upon activation

Catalyst	Component	CN	R (Å)	σ^2/Å^2	E_0 shift (eV)	R-factor
Pd_3/Al_2O_3	Pd–P	2.9 (3)	2.250 (2)	0.0063 (1)	1.1 (2)	**0.019**
	Pd–Cl	0.7 (3)	2.312 (3)	0.0058 (3)		
	Pd–Pd	1.8 (1)	2.98 (1)	0.0101 (5)		
Pd_3/Al_2O_3–$NaBH_4$(A)	Pd–O	3.3 (1)	2.009 (1)	0.0028 (2)	5.3 (2)	**0.004**
	Pd–Pd	1.1 (1)	2.65 (1)	0.010 (2)		
Pd_3/Al_2O_3–$NaBH_4$(B)	Pd–O	2.8 (1)	1.99 (1)	0.0043 (2)	9.2 (7)	**0.003**
	Pd–B	2.3 (6)	1.87 (3)	0.005 (4)		
	Pd–Pd	2.4 (3)	2.762 (7)	0.010 (1)		
Pd_3/Al_2O_3–$NaBH_4$(C)	Pd–O	1.4 (3)	2.01 (3)	0.0048 (2)	9.6 (5)	**0.014**
	Pd–B	3.3 (1)	1.98 (2)	0.006 (2)		
	Pd–Pd	4.0 (5)	2.781 (3)	0.009 (3)		
Pd_3/Al_2O_3–$LiBH_4$(A)	Pd–O	2.3 (1)	2.014 (4)	0.0021 (6)	2.4 (8)	**0.016**
	Pd–Pd	2.0 (5)	2.74 (1)	0.012 (9)		
Pd_3/Al_2O_3–$LiBH_4$(B)	Pd–O	2.7 (1)	2.006 (2)	0.0022 (3)	−2.5 (2)	**0.007**
	Pd–Pd	2.3 (1)	2.727 (4)	0.0075 (4)		
Pd_3/Al_2O_3–$LiBH_4$(C)	Pd–O	2.4 (1)	2.000 (3)	0.0027 (5)	3.2 (3)	**0.012**
	Pd–Pd	2.5 (1)	2.725 (5)	0.0073 (6)		
Pd_3/Al_2O_3–$LiAlH_4$(A)	Pd–O	2.5 (1)	2.017 (3)	0.0025 (5)	4.7 (4)	**0.017**
	Pd–Pd	0.5 (2)	2.68 (3)	0.011 (4)		
Pd_3/Al_2O_3–$LiAlH_4$(B)	Pd–O	2.8 (1)	2.008 (3)	0.0024 (4)	4.6 (4)	**0.019**
	Pd–Pd	0.6 (1)	2.69 (2)	0.007 (2)		
Pd_3/Al_2O_3–$LiAlH_4$(C)	Pd–O	2.5 (1)	2.013 (2)	0.0024 (3)	4.1 (4)	**0.022**
	Pd–Pd	0.5 (1)	2.69 (2)	0.008 (2)		

actions can be attributed to reduced metal–support interactions as the size of the supported NPs increased.

For the $LiBH_4$-activated samples (Pd_3/Al_2O_3–$LiBH_4$(A/B/C)), the CN for the Pd–O interaction was in the 2.3–2.7 range for the three samples, while the CN for Pd–Pd interactions was 2.0 ± 0.5, 2.3 ± 0.1, and 2.5 ± 0.1 for Pd_3/Al_2O_3–$LiBH_4$(A), Pd_3/Al_2O_3–$LiBH_4$(B), and Pd_3/Al_2O_3–$LiBH_4$(C), respectively. This suggests a very slight growth of NCs after $LiBH_4$ treatment. Similar to $LiBH_4$-activated samples, the CN of Pd–O in samples activated by $LiAlH_4$ (Pd_3/Al_2O_3–$LiAlH_4$(A/B/C)) was found to be around 2.5–2.8 for the three samples. However, the Pd–Pd interactions showed a significantly lower CN of approximately 0.5 in the fitting of these samples. This indicates a substantial disruption of Pd–Pd bonds in the triangular metal core of Pd_3 NCs upon $LiAlH_4$ activation. This is consistent with the possibility of a mixture of Pd NCs and single-atom sites in the $LiAlH_4$-activated samples. Unlike the $NaBH_4$ and $LiBH_4$-treated samples, no correlation between the loadings of the reducing agent and the resulting Pd–Pd CN of the activated NCs has been observed in the case of samples activated *via* $LiAlH_4$. Overall, the XAS results showed that all the reducing agents can activate Pd_3 NCs by removing phosphine and chloride ligands from their surfaces. After activation, the Pd atoms interact with oxygen atoms on the surface of γ-Al_2O_3. In the case of $NaBH_4$ and $LiBH_4$-activated samples, the structure and morphology of the NCs upon activation depend on the amount of reducing agent used.

XPS analysis was conducted on activated Pd_3/Al_2O_3 samples to investigate the speciation of Pd and validate the presence of B atoms in the samples. The Pd 3d region of XPS spectra for Pd_3/Al_2O_3, Pd_3/Al_2O_3–$NaBH_4$(A/B/C), and Pd_3/Al_2O_3–$LiAlH_4$(A/B/C), along with the Cl 2p, B 1s, and P 2s regions of Pd_3/Al_2O_3–$NaBH_4$(A/B/C) have been shown in Fig. 2. The Pd 3d

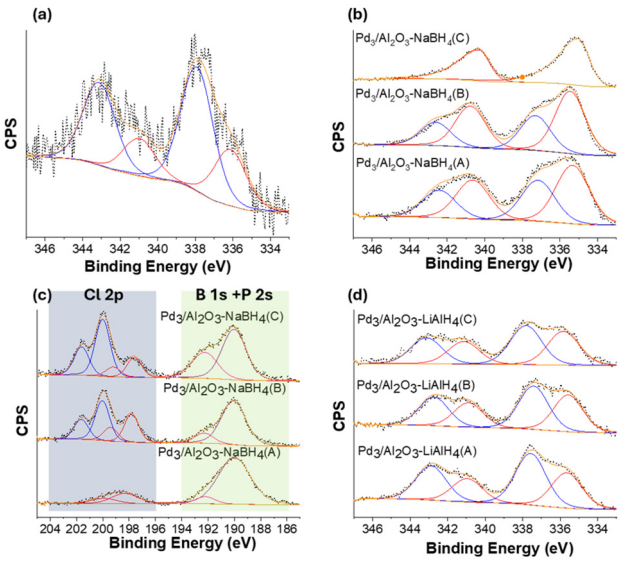

Fig. 2 (a) XPS Pd 3d spectra of Pd_3/Al_2O_3, XPS Pd 3d spectra of Pd_3/Al_2O_3 catalysts treated with (b) $NaBH_4$, and (d) $LiAlH_4$; black dots and orange solid lines represent the experiment data and fit respectively; red lines represent the $3d_{5/2}$ (right) and $3d_{3/2}$ (left) regions for Pd(0); blue lines represent the $3d_{5/2}$ (right) and $3d_{3/2}$ (left) regions for Pd(II). (c) XPS Cl 2p + B 1s + P 2s spectra of Pd_3/Al_2O_3 catalysts treated with $NaBH_4$; black dots and orange solid lines represent the experiment data and fit respectively; red lines represent the $2p_{3/2}$ (right) and $2p_{1/2}$ (left) regions for the first Cl component; blue lines represent the $2p_{3/2}$ (right) and $2p_{1/2}$ (left) regions for the second Cl component; purple lines represent the P 2s region and pink lines represent the B 1s region.

XPS spectra of the Pd_3/Al_2O_3 showed peaks corresponding to two components of Pd, with $3d_{5/2}$ peaks at approximately 336.1 and 338.0 eV and an area ratio close to 1 : 2, consistent

with XPS results reported in the literature (Fig. 2a).[16] In the case of the samples activated using $NaBH_4$ (Pd_3/Al_2O_3–$NaBH_4$(A/B/C)), two species of Pd can be seen in the XPS spectra *i.e.*, Pd(0) and Pd(II) with Pd $3d_{5/2}$ peaks at around 335.3 and 337.2 eV respectively (Fig. 2b). The fraction of Pd(0) relative to Pd(II) can be seen increasing with the amount of $NaBH_4$ used for the activation progressing from Pd_3/Al_2O_3–$NaBH_4$(A) to Pd_3/Al_2O_3–$NaBH_4$(C), which can be due to reduction of Pd(II) to Pd(0) upon exposure to $NaBH_4$. For Pd_3/Al_2O_3–$NaBH_4$(C), the XPS spectra only showed Pd(0), with the Pd(II) fraction completely absent. This observation is consistent with the XAS analysis, which indicated that the size of the Pd NPs increased at higher $NaBH_4$ loadings, while the interaction of Pd atoms with the O atoms of the γ-Al_2O_3 decreased. The interaction of Pd with surface O of γ-Al_2O_3 likely accounts for the presence of the high-valent Pd(II) species. The absence of high valent Pd(II) species in the XPS data for the Pd_3/Al_2O_3–$NaBH_4$(C) sample may be due to the presence of buried Pd–O interfaces for the larger Pd NPs (as EXAFS data shows a Pd–O CN of 1.4(3) for this sample).

While Pd–P and Pd–Cl interactions were not present in the EXAFS spectra of the Pd_3/Al_2O_3–$NaBH_4$(A/B/C), in the XPS analysis, peaks for phosphine and chloride species can be observed for these samples (Fig. 2c). Most likely, these ligands were adsorbed onto the surface of γ-Al_2O_3 after being removed from the metal core of Pd_3 NCs during the activation. In the literature, thiolate-protected $Au_{25}(SR)_{18}$ and $Ag_{25}(SR)_{18}$ NCs have been reported to exhibit similar behavior during thermal activation on a solid support.[18,35] A very weak feature in the Cl 2p region of Pd_3/Al_2O_3–$NaBH_4$(A) can be seen with the Cl $2p_{3/2}$ peak at 198.3 eV. With further increase in the concentration of the $NaBH_4$ for the activation *i.e.*, Pd_3/Al_2O_3–$NaBH_4$(B/C), peaks for two distinct components of Cl can be observed with Cl $2p_{3/2}$ peak position at 197.6 and 200.0 eV. The peak at around 197.6 eV can be assigned to NaCl and the peak at around 200.0 eV is likely due to the interaction between Al and Cl.[36,37] A strong P 2s signal in the samples can be seen at *ca.* 190 eV. The B 1s region in the XPS is very close to the P 2s region. In the case of Pd_3/Al_2O_3–$NaBH_4$(A/B/C), a B 1s component in the XPS spectra at around 192.3 eV (Fig. 2c) has been fitted. The hydrolysis of $NaBH_4$ typically produces borates as side products,[38] and the location of the B 1s peak in the spectra of the activated samples is close to that of the reported shift of sodium tetraborate (*i.e.*, 192.6 eV).[36] Therefore this peak can be assigned to tetraborate side products adsorbed on the γ-Al_2O_3 support. The relative peak area of this 192.3 eV B 1s peak increased with higher amounts of $NaBH_4$ used for activation. This suggests that higher amounts of the reducing agent resulted in greater adsorption of tetraborate species on the surface of the γ-Al_2O_3. While XAS studies indicated that B also begins to intercalate into Pd NPs at large $NaBH_4$ excesses, a separate B 1s peak for this species can not be assigned, which is likely due to overlap with the large P 2s signal present at 190 eV.

Similar to Pd_3/Al_2O_3–$NaBH_4$(A/B), the Pd 3d XPS spectrum of Pd_3/Al_2O_3–$LiBH_4$(B) (Fig. S7a†) showed the presence of two Pd components with Pd $3d_{5/2}$ peaks at 335.3 eV for Pd(0) and 337.1 eV for Pd(II). The peak area for the Pd(II) component was found to be slightly lower than that of Pd(0). Conversely, in the case of the $LiAlH_4$-treated samples *i.e.*, Pd_3/Al_2O_3–$LiAlH_4$(A/B/C), the peak area for the Pd(II) component has been found higher than that of Pd(0), indicating that much of the Pd is present in a higher-valent state after activation (Fig. 2d). Moreover, the relative peak areas of Pd 3d regions for Pd_3/Al_2O_3–$LiAlH_4$(A/B/C) did not vary much from each other, suggesting identical speciation of Pd, which is consistent with EXAFS analysis. The Al 2p XPS spectra for the Pd_3/Al_2O_3–$NaBH_4$(A/B/C) and Pd_3/Al_2O_3–$LiAlH_4$(A/B/C) are shown in Fig. S7b and S7c,† respectively. The peak in the Al 2p region at approximately 74.1 eV is consistent with the reported binding energy value of γ-Al_2O_3.[39] The Al 2p region did not show the appearance of any new peaks after treatment with the reducing agents, suggesting that the surface γ-Al_2O_3 remained unchanged during the reducing agent treatments.

To validate the presence of adsorbed side products of B in the $NaBH_4$-and $LiBH_4$-activated samples, solid-state ^{11}B magic angle spinning (MAS) NMR analysis was performed on Pd_3/Al_2O_3–$NaBH_4$(A/B/C) and Pd_3/Al_2O_3–$LiBH_4$(B) samples (Fig. 3). The ^{11}B MAS NMR spectra of all the activated NCs showed three peaks at 15.6, 10.5, and 1.3 ppm. The positions and shapes of these peaks are in good agreement with those of sodium tetraborate reported in the literature.[40] This indicates that during the activation of Pd_3 NCs, $NaBH_4$ and $LiBH_4$ formed tetraborate (or related species) as a side product and remained adsorbed onto the γ-Al_2O_3 surface even after several washing cycles. Similar peaks were seen for a control sample in which γ-Al_2O_3 was treated with $NaBH_4$ in the absence of Pd_3 NCs (Fig. 3a). For the Pd_3/Al_2O_3–$NaBH_4$(B) sample, a new small peak was found around 5.8–5.9 ppm in ^{11}B MAS NMR, which increased in intensity further for the Pd_3/Al_2O_3–$NaBH_4$(C) sample. Chan *et al.* reported a similar shift for the peaks of intercalated or surface B in fcc Pd.[31] Therefore, the

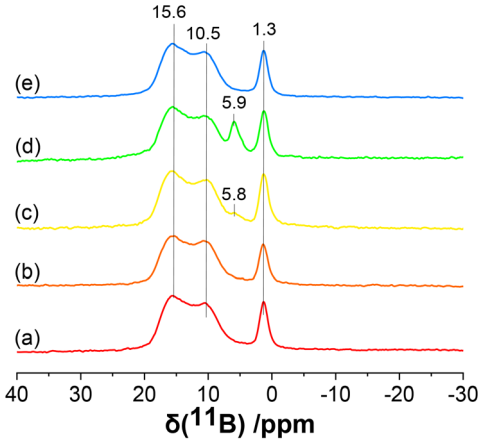

Fig. 3 ^{11}B MAS NMR of (a) Al_2O_3–$NaBH_4$(C) control, (b) Pd_3/Al_2O_3–$NaBH_4$(A), (c) Pd_3/Al_2O_3–$NaBH_4$(B), (d) Pd_3/Al_2O_3–$NaBH_4$(C) and (e) Pd_3/Al_2O_3–$LiBH_4$(B).

peak at 5.9 ppm in ^{11}B MAS NMR was attributed to the intercalated B atoms inside the Pd lattice, which is consistent with EXAFS data showing Pd–B interactions in these samples. However, the new peak for intercalated B was not seen for the $LiBH_4$-treated samples, showing that there was no B incorporation in the Pd NCs, likely because of the smaller concentrations of $LiBH_4$ used for the activation compared to $NaBH_4$. These results are consistent with the absence of a Pd–B interaction in the EXAFS data for the $LiBH_4$-activated samples. Finally, ^{31}P MAS NMR of these samples also indicated the complete removal of phosphine ligands from the Pd_3 NCs, however, peaks for remaining phosphine impurities on the surface of the γ-Al_2O_3 after activation were present (Fig. S8†).

HAADF-STEM analyses of the activated samples were performed to investigate the size, shape, and distribution of the NCs upon activation (Fig. 4). The Pd_3 NCs appeared to be well-dispersed on the surface of the γ-Al_2O_3 (Fig. 4a), with an average NC size of 0.9 ± 0.3 nm. Upon activation with low amounts of $NaBH_4$, the average NC size was 0.8 ± 0.4 nm for Pd_3/Al_2O_3–$NaBH_4$(A) (Fig. 4b). In contrast, for Pd_3/Al_2O_3–$NaBH_4$(B), an increase in Pd particle size was observed after activation, and Pd NPs with an average size of 3.4 ± 0.8 nm are apparent in both HR-TEM (Fig. S9a†) and HAADF-STEM (Fig. 4c) images. The HAADF-STEM image of Pd_3/Al_2O_3–$LiBH_4$(A) revealed the formation of NCs with an average size of 1.7 ± 0.5 nm (Fig. 4d), while activation with a higher concentration of $LiBH_4$ in Pd_3/Al_2O_3–$LiBH_4$(B) resulted in slightly larger NCs (2.5 ± 0.6 nm) (Fig. S9b† and Fig. 4e). In the HAADF-STEM images of Pd_3/Al_2O_3–$LiAlH_4$(A) (Fig. 4f) and Pd_3/Al_2O_3–$LiAlH_4$(B) (Fig. S10†), Pd NCs with average sizes of approximately 1.1 ± 0.5 nm and 1.5 ± 0.4 nm are apparent. However, it should be noted that the EXAFS fitting revealed a very low Pd–Pd CN of around 0.5 for these samples, which would suggest that the sample contains both NCs and single-atom sites γ-Al_2O_3 surface, the latter of which could not be imaged.

To visualize the dispersion of the Pd particles and borates on the γ-Al_2O_3 support, STEM-EDX elemental mapping analysis of the activated samples was performed. STEM-EDX images of Pd_3/Al_2O_3–$NaBH_4$(A) (Fig. S11†) showed a homogenous distribution of Pd over the surface of the γ-Al_2O_3 support. In the case of Pd_3/Al_2O_3–$NaBH_4$(B), some larger Pd particles can be observed on the γ-Al_2O_3 support in the STEM-EDX images (Fig. S12†). However, in both of these cases (*i.e.*, for Pd_3/Al_2O_3–$NaBH_4$(A/B)), the B density did not seem to be localized near the position of Pd (Fig. S11 and S12†). In the case of Pd_3/Al_2O_3–$NaBH_4$(B), the atomic fraction of B in the provided STEM-EDX image was found to be around 0.23% (Table S2†). We believe the large amount of borates still present on the γ-Al_2O_3 support makes it very difficult to visualize small amounts of B incorporated into the Pd NPs (as evidence by EXAFS and NMR). For Pd_3/Al_2O_3–$LiBH_4$(B), the STEM-EDX maps (Fig. S13†) indicated the random distribution of large Pd NCs with an average size of around 2.6 nm on the γ-Al_2O_3 surface. However, no B signal was detected from this $LiBH_4$-treated sample, likely due to the low concentration of tetraborate species on the γ-Al_2O_3 support (Table S2†). In the case of Pd_3/Al_2O_3–$LiAlH_4$(B), the STEM-EDX maps (Fig. S14†) showed a fairly homogeneous distribution of Pd over the γ-Al_2O_3 surface with a 0.35% Pd loading (Table S2†).

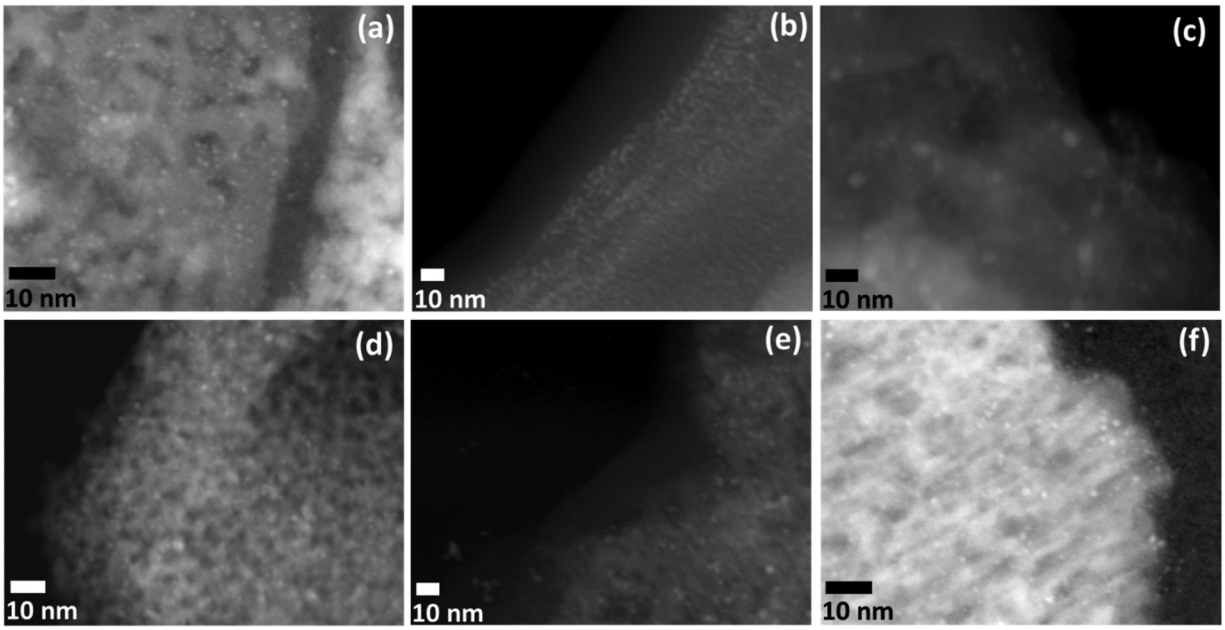

Fig. 4 HAADF-STEM images of (a) Pd_3/Al_2O_3 (avg. Pd size: 0.9 ± 0.3 nm), (b) Pd_3/Al_2O_3–$NaBH_4$(A) (avg. Pd size: 0.8 ± 0.4 nm), (c) Pd_3/Al_2O_3–$NaBH_4$(B) (avg. Pd size: 3.4 ± 0.8 nm), (d) Pd_3/Al_2O_3–$LiBH_4$(A) (avg. Pd size: 1.7 ± 0.5 nm), (e) Pd_3/Al_2O_3–$LiBH_4$(B) (avg. Pd size: 2.5 ± 0.6 nm) and (f) Pd_3/Al_2O_3–$LiAlH_4$(A) (avg. Pd size: 1.1 ± 0.5 nm).

Overall, the results from the combination of the aforementioned techniques indicated that all the used reducing agents are capable of activating the Pd_3 NCs on the γ-Al_2O_3 surface by removing phosphine and chloride ligands from the NC surfaces. Treatment with a low amount of $NaBH_4$ in Pd_3/Al_2O_3–$NaBH_4$(A) led to the activation of Pd_3 NCs without noticeable size growth, while treatment with higher amounts of $NaBH_4$ in Pd_3/Al_2O_3–$NaBH_4$(A/B) resulted in the formation of larger Pd NPs with intercalated B atoms. In the case of $LiBH_4$-treated samples, *i.e.*, Pd_3/Al_2O_3–$LiBH_4$(A/B/C), slightly larger NCs were formed depending on the amount used for activation, and no intercalated B species were seen in the resulting Pd NCs. Finally, activation with $LiAlH_4$ in Pd_3/Al_2O_3–$LiAlH_4$ (A/B/C) resulted in the formation of a mixture of Pd single-atom sites and very small NCs, and the size and distribution of the Pd particles were found to be independent of the amounts of the $LiAlH_4$ used for the activation.

To measure the effect of activation of the Pd_3 NCs on their catalytic activity, the transfer hydrogenation of an α,β-unsaturated aldehyde, *trans*-cinnamaldehyde (CAL), was performed. Selective partial hydrogenation of CAL can yield hydrocinnamaldehyde (HCAL) or cinnamic alcohol (COL), depending on whether the C=C or C=O bonds are hydrogenated, respectively.[41] However, upon complete hydrogenation of both C=C and C=O bonds, hydrocinnamic alcohol (HCOL) can be obtained.[41] The products of this reaction, *i.e.*, HCAL and COL have various applications in the pharmaceutical and fragrance fields.[41] Thermodynamically, hydrogenation of the C=C bond is favoured over the C=O bond due to its lower bond energy.[42] For this transfer hydrogenation reaction, formic acid and its formates have been selected as the hydrogen donors. Due to increased sustainability and cost-effectiveness, biomass-derived hydrogen donors such as formic acid and related formates have attracted research attention in the field of transfer hydrogenation.[43] Formic acid has a very high volumetric capacity for hydrogen storage which can be released by either dehydrogenation or dehydration pathways.[44] However, one major challenge in using formic acid in high concentrations at the industrial level is the corrosion of the reactors; thus, using neutralized acids (*e.g.*, formates) instead of formic acid is more favourable.[43]

The reaction conditions for the transfer hydrogenation of CAL were optimized by using Pd_3/Al_2O_3–$NaBH_4$(A) as a model catalyst at 70 °C for 3 hours (Table 2). The reaction was first examined with formic acid as a hydrogen source and in the absence of a base, which resulted in a very low conversion, *i.e.*, 12.2% (Table 2, entry 1). Upon adding 5 mmol of KOH to the reaction, the conversion increased to 63.4% (Table 2, entry 2). With a decrease in the amount of KOH from 5 mmol to 1 mmol, the conversion dropped by a factor of 2 (Table 2, entry 3). Previously, Lee *et al.* have shown that the decomposition of formic acid over Pd involves the formation and interaction of $HCOO^-$ with the metal center followed by C–H activation *via* β-hydride elimination reaction (Scheme S1†).[45] The use of strong bases as the additive can make this process thermodynamically more favourable as the base can facilitate the formation of $HCOO^-$ species.[44] Changing the solvent from MeOH to EtOH did not have much effect on the conversion (Table 2, entry 4). However, upon using water as a solvent, the conversion dropped significantly to 28.9% (Table 2, entry 5). The

Table 2 Optimization of the reaction conditions for the transfer hydrogenation of CAL using Pd_3/Al_2O_3–$NaBH_4$(A)

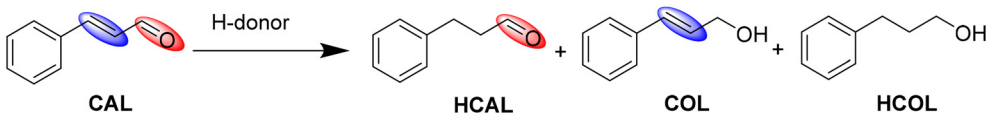

Entry	Hydrogen source/amount (mmol)	Solvent	Additive/amount (mmol)	Conversion%
1	HCOOH/5	MeOH	—	12.2%
2	HCOOH/5	MeOH	KOH/5	63.4%
3	HCOOH/5	MeOH	KOH/1	31.1%
4	HCOOH/5	EtOH	KOH/5	68.3%
5	HCOOH/5	H_2O	KOH/5	28.9%
6	HCOOH/5	H_2O	—	5.3%
7	HCOOH/5	H_2O	NaOH/5	25.7%
8	HCOOH/5	H_2O	K_2CO_3/5	11.4%
9[a]	HCOOH/5	H_2O	KOH/5	0%
10	HCOONa/5	H_2O	—	35.4%
11	HCOONa/5	EtOH	—	62.8%
12	HCOONa/5	MeOH	—	60.8%
13	HCOONa/5	Toluene	—	0%
14	HCOONa/5	EtOH : H_2O (1 : 1)	—	68.7%
15[a]	HCOONa/5	EtOH : H_2O (1 : 1)	—	3.3%
16	HCOONa/10	EtOH : H_2O (1 : 1)	—	73.2%
17	HCOONa/1	EtOH : H_2O (1 : 1)	—	21.0%
18	$HCOONH_4$/5	EtOH : H_2O (1 : 1)	—	63.9%

Reaction conditions: 1.0 mmol of CAL, 4.0 ml of solvent, 25.0 mg of Pd_3/Al_2O_3–$NaBH_4$(A) (Pd mol% = 0.11%) at 70 °C for 3 hours. [a] Reaction was carried out at room temperature. The selectivity for HCAL in all these reactions is between 85–93% with no traceable formation of COL.

main reason behind this large drop is likely the poor solubility of CAL in water. With the absence of the base, the catalysts did not show any significant activity in water (Table 2, entry 6). Upon using the NaOH as a base in water, the catalyst showed 25.7% conversion (Table 2, entry 7). However, upon using a comparatively milder base, *i.e.*, K_2CO_3, the conversion further dropped to 11.4% (Table 2, entry 8). At room temperature, no conversion was obtained in water with formic acid as the hydrogen donor and KOH as the base (Table 2, entry 9). Conversely, sodium formate as a hydrogen donor in the absence of a base provided 35.4% conversion in water (Table 2, entry 10), which further increased to 62.8% and 60.8% upon using EtOH and MeOH as the solvent, respectively (Table 2, entries 11 and 12). The reaction did not show any conversion when toluene was used as the solvent, probably due to the poor solubility of sodium formate in toluene (Table 2, entry 13). The best result, *i.e.*, 68.7% conversion, was obtained using a mixture of water and EtOH as the solvent (Table 2, entry 14). However, at room temperature, the same conditions provided only a 3.3% conversion (Table 2, entry 15). This is likely due to the unfavorable conditions for C–H activation *via* β-hydride elimination at low temperatures (Scheme S1†). Doubling the amount of sodium formate resulted in a slight increase in conversion (Table 2, entry 16). Conversely, reducing the sodium formate to 1 mmol led to a conversion of only 21% (Table 2, entry 17). Finally, ammonium formate as the hydrogen donor gave a conversion rate similar to sodium formate (Table 2, entry 18). Notably, in all of these optimization reactions, no formation of COL was observed, and the selectivity towards HCAL remained consistently high, ranging from 85% to 93% (with HCOL as the other minor product). This suggests that the reaction selectivity remains largely unaffected by varying reaction conditions and is primarily governed by catalyst properties.

After identifying the optimum conditions, non-activated Pd_3/Al_2O_3 and all the activated NCs were employed as catalysts in the transfer hydrogenation of CAL using sodium formate as the hydrogen donor in a 1 : 1 H_2O : EtOH solvent (Table 3). Non-activated Pd_3/Al_2O_3 showed a low conversion of 38.3% with a selectivity of around 78.1% towards HCAL. The activated Pd_3/Al_2O_3–$NaBH_4$(A) catalysts showed improved activity, achieving a conversion rate of 68.7% and an improved selectivity towards HCAL of 90.5%. In the case of Pd_3/Al_2O_3–$NaBH_4$(B) and Pd_3/Al_2O_3–$NaBH_4$(C), the obtained conversions were very high (98.3% and 95.0%, respectively), however, these catalysts showed much lower selectivity towards HCAL and a higher proportion of the completely hydrogenated products, *i.e.*, HCOL, formed. This result is consistent with the larger size of the Pd NPs under these activation conditions, and the higher activity may also be enhanced due to B-incorporation into the Pd NPs. Previously, it has been shown in the literature that the intercalation of B inside the Pd lattice can boost their efficiency in hydrogen generation from formic acid.[46–48] As these samples also contained the B intercalated Pd particles, their higher catalytic activity for the transfer hydrogenation of CAL is likely associated with their enhanced capability of extracting hydrogen from formate species during catalysis. Pd_3/Al_2O_3–$LiBH_4$(A/B/C) catalysts demonstrated reasonable conversions between 63–73% coupled with high selectivity of around 90% towards HCAL. This is consistent with the moderate NC sizes seen after $LiBH_4$ activation (1.7–2.5 nm) as evidenced by EXAFS and HAADF-STEM analyses. In contrast, Pd_3/Al_2O_3–$LiAlH_4$(A/B/C) catalysts showed slightly lower conversions, ranging from 49.6–61.1%, with selectivities towards

Table 3 Catalytic performance of the activated catalysts for the transfer hydrogenation of CAL

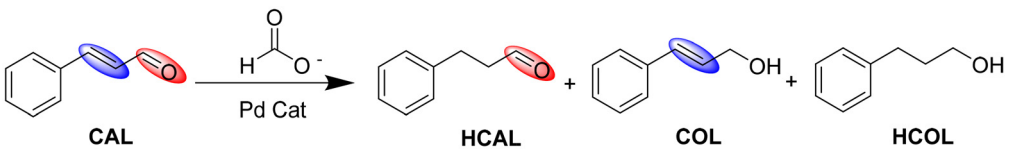

Catalyst	Conversion, %	Selectivity, %		
		HCAL	COL	HCOL
Pd_3/Al_2O_3	38.3%	78.1%	≤0.1%	21.9%
Pd_3/Al_2O_3–$NaBH_4$(A)	68.7%	90.5%	≤0.1%	9.4%
Pd_3/Al_2O_3–$NaBH_4$(B)	98.3%	71.2%	≤0.1%	28.7%
Pd_3/Al_2O_3–$NaBH_4$(C)	95.0%	67.1%	≤0.1%	32.9%
Pd_3/Al_2O_3–$LiBH_4$(A)	69.3%	91.2%	≤0.1%	8.7%
Pd_3/Al_2O_3–$LiBH_4$(B)	72.3%	89.9%	≤0.1%	9.9%
Pd_3/Al_2O_3–$LiBH_4$(C)	63.3%	93.2%	≤0.1%	6.8%
Pd_3/Al_2O_3–$LiAlH_4$(A)	57.3%	91.3%	≤0.1%	8.6%
Pd_3/Al_2O_3–$LiAlH_4$(B)	49.6%	90.0%	≤0.1%	9.9%
Pd_3/Al_2O_3–$LiAlH_4$(C)	61.1%	94.0%	≤0.1%	5.8%
Pd_3/Al_2O_3-150	37.2%	96.0%	≤0.1%	4.0%

Reaction conditions: 1.0 mmol of CAL, 5.0 mmol of HCOONa, 4 ml of solvent (1 : 1 H_2O : EtOH), 25.0 mg of catalyst (Pd mol% = 0.11%) at 70 °C for 3 hours.

HCAL exceeding 90%. Based on EXAFS and HAADF-STEM results, these catalysts consist of a combination of single-atom sites and small NCs ranging in size from 1.1 to 1.5 nm. Consequently, due to the small size of the Pd NCs, these catalysts exhibited lower catalytic activity but higher selectivity towards HCAL. To compare the catalytic performance of the chemically activated NCs with thermally activated NCs, Pd_3/Al_2O_3 was treated at 150 °C for 3 hours to obtain Pd_3/Al_2O_3-150.[16] Previously, it has been found that after thermal activation at 150 °C, phosphines on the Pd_3 NCs can be effectively removed without any increase in NC size on activated carbon supports; but the resulting Pd_3 NCs have significant Pd–Cl interactions.[16] In the hydrogenation of CAL, Pd_3/Al_2O_3-150 exhibited a relatively lower conversion of 37.2% along with a very high selectivity towards HCAL. The lower activity of the thermally activated sample may be due to the presence of Cl ligands on the surface of NCs after thermal treatment.[16]

None of the catalysts exhibited significant formation of COL, consistent with previous work on Pd-based nano-sized catalysts.[41,49,50] In the hydrogenation of CAL, the Pd-based catalysts are mainly selective towards HCAL, however, other noble metals such as Pt, Au, and Ir are more selective towards the formation of COL.[41,49,50] This implies that the η^4 adsorption mode of CAL is preferred over the Pd surface of these catalysts, which leads to the hydrogenation of the C=C bond followed by the hydrogenation of the C=O bond.[41] Previously, Liu and coworkers demonstrated through DFT calculations that the adsorption energy of the C=C bond on Pd_4 NCs is lower than that of the C=O bond, whereas, larger Pd particles with Pd(111) surfaces exhibit stronger C=O bond adsorption.[51] Thus, smaller Pd NCs are more selective for the conversion of CAL to HCAL. In recent work on di-1-adamantylphosphine-stablized Pd_n (n = 2–5) NCs supported on carbon,[52] Tang *et al.* noted that the Pd_5 NCs exhibited high selectivity (95.3%) towards HCAL formation at a high conversion in the hydrogenation of CAL. Conversely, Pd_2 NCs analogs showed significantly lower activity but maintained a high selectivity of 99.9% towards HCAL, while Pd_3 NCs achieved complete conversion but a lower selectivity (80.5%) towards HCAL.[52] These results indicated that changes in both the particle size and electronic structure of the Pd_n NCs significantly influenced their activity and selectivity.[51,52] Recent work by Li *et al.* showed that the carbon-nitride-nanosheet-supported Pd NCs along with Pd single-atom sites led to a complete conversion in the hydrogenation of CAL with a 97.3% selectivity towards HCAL.[53] Using DFT calculations, a synergistic effect between single atom sites and NCs was found, where the CAL is preferentially adsorbed on Pd single-atom sites and hydrogen adsorbed on NCs.[53] In the case of Pd_3/Al_2O_3–$LiAlH_4$(A/B/C), a mix of NCs and atomically dispersed Pd sites were observed, however, the conversions for these catalysts were somewhat lower compared to the reported results for this similar system.[53] This may be due to a non-uniform distribution of the Pd sites on the γ-Al_2O_3 support in comparison to the homogenous distribution of Pd sites on g-C_3N_4.[53] Overall the catalytic results in this manuscript showed that the post-activation evolution of NCs has a direct effect on the activity and selectivity of the catalysts. Larger Pd NPs have shown higher activity for the transfer hydrogenation reactions, likely due to the presence of well-faceted Pd(111) surfaces and the presence of intercalated B species in the Pd NPs. However, the presence of Pd(111) surfaces also led to strong adsorption of the substrate on the metal surface resulting in the increased formation of a completely hydrogenated product.[54] However, in the case of small-size NCs and single-atom sites, the activity has been found lower due to weaker interactions of the catalyst with the substrates, which leads to higher selectivity toward the partially hydrogenated product, HCAL.

Conclusions

This work demonstrates the chemical activation of the γ-Al_2O_3-supported Pd_3 NCs using various hydride-based reducing agents for transfer hydrogenation reactions. Different amounts of $NaBH_4$, $LiBH_4$, and $LiAlH_4$ were used for activation, and the post-activation structural evolution of the NCs was monitored using a combination of various techniques. XAS results indicate that all reducing agents effectively removed surface phosphine and chloride ligands from Pd_3 NCs. Both XAS and HAADF-STEM analyses showed that lower amounts of $NaBH_4$ activated the Pd_3 NCs without any noticeable size growth, while higher $NaBH_4$ amounts caused a transformation of Pd NCs into Pd NPs. XPS, solid-state NMR, and STEM-EDX analyses revealed the presence of tetraborate and phosphine impurities on the surface of γ-Al_2O_3, even after post-activation washings in the $NaBH_4$-treated samples. Additionally, solid-state NMR and EXAFS analysis suggested the intercalation of B atoms within the lattice of formed Pd NPs for samples activated with high $NaBH_4$ loadings. Activation with $LiBH_4$ resulted in a slight increase in the size of the Pd NCs, producing NCs ranging from 1.7 to 2.5 nm in size. Activation with $LiAlH_4$ converted Pd_3 NCs into a mixture of single-atom sites and small NCs around 1.4 nm in size. The post-activation evolution of Pd_3 NCs directly impacted their catalytic behavior in the transfer hydrogenation of CAL. Smaller Pd NCs were highly selective towards the formation of HCAL, the partial hydrogenation product, whereas larger Pd NPs were more active catalysts, but also increased the complete hydrogenation of CAL to HCOL. Overall, our results demonstrate that immobilizing atom-precise Pd_3 NCs onto an γ-Al_2O_3 support followed by chemical activation is an effective method to obtain supported Pd NCs for heterogeneous catalysis. This approach offers greater control over the structure and speciation of the Pd NCs compared to traditional thermal activation methods.

Author contributions

All authors have approved the final version of the manuscript. S. S. and R. W. J. S. contributed to the initial concept development, experimental design, characterization of catalysts, analysis of results, and writing of the

manuscript. D. W. carried out catalytic studies under the supervision of S. S. HR-TEM, HAADF-STEM and STEM-EDX analysis has been carried out by K. E. S. under the supervision of D. H.

Data availability

The data supporting this article have been included as part of the ESI.†

Conflicts of interest

There are no conflicts to declare.

Acknowledgements

We acknowledge financial assistance from the National Sciences and Engineering Research Council of Canada. We thank Ning Chen and Weifeng Chen at the HXMA beamline (Canadian Light Source) for their assistance in XAS measurements. XAS experiments were performed at the Canadian Light Source, a national research facility of the University of Saskatchewan, which is supported by the Canada Foundation for Innovation, the National Sciences and Engineering Research Council of Canada, the National Research Council, the Canadian Institutes of Health Research, the Government of Saskatchewan, and the University of Saskatchewan. The Saskatchewan Structural Sciences Centre (SSSC) is acknowledged for providing NMR and XPS facilities to conduct this research. Sarah Purdy and Jianfeng Zhu at SSSC are acknowledged for their assistance with XPS and solid-state NMR analysis, respectively. Funding from the Canada Foundation for Innovation, Natural Sciences and Engineering Research Council of Canada, and the University of Saskatchewan support research at the SSSC. Electron microscopy was performed at the Canadian Centre for Electron Microscopy at McMaster University.

References

1 C. Dong, Z. Gao, Y. Li, M. Peng, M. Wang, Y. Xu, C. Li, M. Xu, Y. Deng, X. Qin and F. Huang, *Nat. Catal.*, 2022, **5**, 485–493.
2 F. Huang, Y. Deng, Y. Chen, X. Cai, M. Peng, Z. Jia, P. Ren, D. Xiao, X. Wen, N. Wang and H. Liu, *J. Am. Chem. Soc.*, 2018, **140**, 13142–13146.
3 C. Dong, Y. Li, D. Cheng, M. Zhang, J. Liu, Y. G. Wang, D. Xiao and D. Ma, *ACS Catal.*, 2020, **10**, 11011–11045.
4 I. Cano, A. Weilhard, C. Martin, J. Pinto, R. W. Lodge, A. R. Santos, G. A. Rance, E. H. Åhlgren, E. Jónsson, J. Yuan and Z. Y. Li, *Nat. Commun.*, 2021, **12**, 4965.
5 X. Li, S. Mitchell, Y. Fang, J. Li, J. Perez-Ramirez and J. Lu, *Nat. Rev. Chem.*, 2023, **7**, 754–767.
6 N. Jeddi, N. W. J. Scott, T. Tanner, S. K. Beaumont and I. J. S. Fairlamb, *Chem. Sci.*, 2024, **15**, 2763–2777.
7 T. I. Levchenko, H. Yi, M. D. Aloisio, N. K. Dang, G. Gao, S. Sharma, C. Dinh and C. M. Crudden, *ACS Catal.*, 2024, **14**, 4155–4163.
8 D. Yazaki, T. Kawawaki, D. Hirayama, M. Kawachi, K. Kato, S. Oguchi, Y. Yamaguchi, S. Kikkawa, Y. Ueki, S. Hossain, D. J. Osborn, F. Ozaki, S. Tanaka, J. Yoshinobu, G. F. Metha, S. Yamazoe, A. Kudo, A. Yamakata and Y. Negishi, *Small*, 2023, **19**, 2208287.
9 R. Jin, C. Zeng, M. Zhou and Y. Chen, *Chem. Rev.*, 2016, **116**, 10346–10413.
10 V. Sudheeshkumar, K. O. Sulaiman and R. W. J. Scott, *Nanoscale Adv.*, 2020, **2**, 55–69.
11 K. K. Li, C. Wu, T. Yang, D. Qin and Y. Xia, *Acc. Chem. Res.*, 2023, **56**, 1517–1527.
12 T. Kawawaki, Y. Kataoka, M. Hirata, Y. Iwamatsu, S. Hossain and Y. Negishi, *Nanoscale Horiz.*, 2021, **6**, 409–448.
13 N. W. J. Scott, M. J. Ford, N. Jeddi, A. Eyles, L. Simon, A. C. Whitwood, T. Tanner, C. E. Willans and I. J. S. Fairlamb, *J. Am. Chem. Soc.*, 2021, **143**, 9682–9693.
14 N. W. J. Scott, M. J. Ford, C. Schotes, R. R. Parker, A. C. Whitwood and I. J. S. Fairlamb, *Chem. Sci.*, 2019, **10**, 7898–7906.
15 Y. Yun, H. Sheng, J. Yu, L. Bao, Y. Du, F. Xu, H. Yu, P. Li and M. Zhu, *Adv. Synth. Catal.*, 2018, **360**, 4731–4743.
16 S. Singh, K. O. Sulaiman, Mahwar and R. W. J. Scott, *Catal. Sci. Technol.*, 2024, **14**, 322–333.
17 K. O. Sulaiman, M. Zubair, G. King, N. Bedford and R. W. J. Scott, *Phys. Chem. Chem. Phys.*, 2022, **24**, 24834–24844.
18 K. O. Sulaiman, V. Sudheeshkumar and R. W. J. Scott, *RSC Adv.*, 2019, **9**, 28019–28027.
19 Y. Liu, H. Tsunoyama, T. Akitab and T. Tsukuda, *Chem. Commun.*, 2010, **46**, 550–552.
20 V. Sudheeshkumar, M. Lavier, B. Lukan, J. Shen, N. Semagina and R. W. J. Scott, *Catal. Today*, 2023, **407**, 223–229.
21 J. Kilmartin, R. Sarip, R. Grau-Crespo, D. D. Tommaso, G. Hogarth, C. Prestipino and G. Sankar, *ACS Catal.*, 2012, **2**, 957–963.
22 G. Collins, F. Davitt, C. Dwyer and J. D. Holmes, *ACS Appl. Nano Mater.*, 2018, **1**, 7129–7138.
23 S. Das, A. Goswami, M. Hesari, J. F. Al-Sharab, E. Mikmeková, F. Maran and T. Asefa, *Small*, 2014, **10**, 1473–1478.
24 M. Dasog, W. Hou and R. W. J. Scott, *Chem. Commun.*, 2011, **47**, 8569–8571.
25 A. Shivhare and R. W. J. Scott, *RSC Adv.*, 2016, **6**, 62579–62584.
26 S. M. Ansar, F. S. Ameer, W. Hu, S. Zou, C. U. Pittman and D. Zhang, *Nano Lett.*, 2013, **13**, 1226–1229.
27 F. Fu, J. Xiang, H. Cheng, L. Cheng, H. Chong, S. Wang, P. Li, S. Wei, M. Zhu and Y. Li, *ACS Catal.*, 2017, **7**, 1860–1867.

28 T. J. Penfold, I. Tavernelli, C. J. Milne, M. Reinhard, A. E. Nahhas, R. Abela, U. Rothlisberger and M. Chergui, *J. Chem. Phys.*, 2013, **138**, 014104.
29 J. Wang, Y. Kang, H. Yang and W. Cai, *J. Phys. Chem. C*, 2009, **113**, 8366–8372.
30 J. Li, J. Chen, Q. Wang, W. Cai and S. Chen, *Chem. Mater.*, 2017, **29**(23), 10060–10067.
31 C. W. A. Chan, A. H. Mahadi, M. M. Li, E. C. Corbos, C. Tang, G. Jones, W. C. H. Kuo, J. Cookson, C. M. Brown, P. T. Bishop and S. C. E. Tsang, *Nat. Commun.*, 2014, **5**, 5787.
32 A. Leineweber, T. G. Berger, A. Udyansky and V. N. Bugaev, *Z. Kristallogr. – Cryst. Mater.*, 2014, **229**, 353–367.
33 T. T. Zhuang, D. H. Nam, Z. Wang, H. H. Li, C. M. Gabardo, Y. Li, Z. Q. Liang, J. Li, X. J. Liu, B. Chen and W. R. Leow, *Nat. Commun.*, 2019, **10**, 4807.
34 A. P. Deziel, S. Gahlawat, N. Hazari, K. H. Hopmann and B. Q. Mercado, *Chem. Sci.*, 2023, **14**, 8164–8179.
35 B. Zhang, A. Sels, G. Salassa, S. Pollitt, V. Truttmann, C. Rameshan, J. Llorca, W. Olszewski, G. Rupprechter, T. Bürgi and N. Barrabés, *ChemCatChem*, 2018, **10**, 5372–5376.
36 C. D. Wagner, A. V. Naumkin, A. Kraut-Vass, J. W. Allison, C. J. Powell and J. R. Rumble Jr., *NIST Standard Reference Database 20, Version 3.4 (web version)*, 2003 (**https://srdata.nist.gov/xps/**).
37 X. Yang, D. Kim, D. Um, G. Kim and C. Kim, *J. Vac. Sci. Technol., A*, 2009, **27**, 821–825.
38 C. Su, M. Lu, S. Wang and Y. Huang, *RSC Adv.*, 2012, **2**, 2073–2079.
39 B. R. Strohmeier, *Surf. Sci. Spectra*, 1994, **3**, 135–140.
40 W. R. Gunther, Y. Wang, Y. Ji, V. K. Michaelis, S. T. Hunt, R. G. Griffin and Y. Román-Leshkov, *Nat. Commun.*, 2012, **3**, 1109.
41 X. Wang, X. Liang, P. Geng and Q. Li, *ACS Catal.*, 2020, **10**, 2395–2412.
42 P. Gallezot and D. Richard, *Catal. Rev.: Sci. Eng.*, 1998, **40**, 81–126.
43 R. Nie, Y. Tao, Y. Nie, T. Lu, J. Wang, Y. Zhang, X. Lu and C. C. Xu, *ACS Catal.*, 2021, **11**, 1071–1095.
44 A. K. Singh, S. Singh and A. Kumar, *Catal. Sci. Technol.*, 2016, **6**, 12–40.
45 W. J. Lee, Y. J. Hwang, J. Kim, H. Jeong and C. W. Yoon, *ChemPhysChem*, 2019, **20**, 1382–1391.
46 Z. Li, J. Xu, F. Meng, K. Yang and D. Lin, *ACS Appl. Mater. Interfaces*, 2022, **14**, 30735–30745.
47 J. S. Yoo, Z. Zhao, J. K. Nørskov and F. Studt, *ACS Catal.*, 2015, **5**, 6579–6586.
48 K. Jiang, K. Xu, S. Zou and W. Cai, *J. Am. Chem. Soc.*, 2014, **136**, 4861–4864.
49 S. Fujiwara, N. Takanashi, R. Nishiyabua and Y. Kubo, *Green Chem.*, 2014, **16**, 3230–3236.
50 Y. Zhao, M. Liu, B. Fan, Y. Chen, W. Lv, N. Lu and R. Li, *Catal. Commun.*, 2014, **57**, 119–123.
51 F. Jiang, J. Cai, B. Liu, Y. Xu and X. Liu, *RSC Adv.*, 2016, **6**, 75541–75551.
52 J. Tang, T. Ge, W. Wang, C. Liu and J. Huang, *Chem. Commun.*, 2023, **59**, 8854–8857.
53 X. Li, J. Liu, J. Wu, L. Zhang, D. Cao and D. Cheng, *ACS Catal.*, 2024, **14**, 2369–2379.
54 X. Zhao, Y. Chang, W. Chen, Q. Wu, X. Pan, K. Chen and B. Weng, *ACS Omega*, 2022, **7**, 17–31.